Whole-Body Biodistribution Kinetics, Metabolism, and Radiation Dosimetry Estimates of ^{18}F-PEG$_6$-IPQA in Nonhuman Primates

Mei Tian[1], Kazuma Ogawa[1], Richard Wendt[2], Uday Mukhopadhyay[1], Julius Balatoni[1], Nobuyoshi Fukumitsu[1], Rajesh Uthamanthil[3], Agatha Borne[3], David Brammer[3], James Jackson[4], Osama Mawlawi[2], Bijun Yang[1], Mian M. Alauddin[1], and Juri G. Gelovani[1]

[1]*Department of Experimental Diagnostic Imaging, The University of Texas MD Anderson Cancer Center, Houston, Texas;* [2]*Department of Imaging Physics, The University of Texas MD Anderson Cancer Center, Houston, Texas;* [3]*Department of Veterinary Medicine and Surgery, The University of Texas MD Anderson Cancer Center, Houston, Texas; and* [4]*Department of Nuclear Medicine, The University of Texas MD Anderson Cancer Center, Houston, Texas*

We recently developed the radiotracer 4-[(3-iodophenyl)amino]-7-(2-[2-{2-(2-[2-{2-(18F-fluoroethoxy)-ethoxy}-ethoxy]-ethoxy)-ethoxy}-ethoxy]-quinazoline-6-yl-acrylamide) (^{18}F-PEG$_6$-IPQA) for noninvasive detection of active mutant epidermal growth factor receptor kinase-expressing non–small cell lung cancer xenografts in rodents. In this study, we determined the pharmacokinetics, biodistribution, metabolism, and radiation dosimetry of ^{18}F-PEG$_6$-IPQA in nonhuman primates. **Methods:** Six rhesus macaques were injected intravenously with 141 ± 59.2 MBq of ^{18}F-PEG$_6$-IPQA, and dynamic PET/CT images covering the thoracoabdominal area were acquired for 30 min, followed by whole-body static images at 60, 90, 120, and 180 min. Blood samples were obtained from each animal at several time points after radiotracer administration. Radiolabeled metabolites in blood and urine were analyzed using high-performance liquid chromatography. The ^{18}F-PEG$_6$-IPQA pharmacokinetic and radiation dosimetry estimates were determined using volume-of-interest analysis of PET/CT image datasets and blood and urine time–activity data. **Results:** ^{18}F-PEG$_6$-IPQA exhibited rapid redistribution and was excreted via the hepatobiliary and urinary systems. ^{18}F-PEG$_6$ was the major radioactive metabolite. The critical organ was the gallbladder, with an average radiation-absorbed dose of 0.394 mSv/MBq. The other key organs with high radiation doses were the kidneys (0.0830 mSv/MBq), upper large intestine wall (0.0267 mSv/MBq), small intestine (0.0816 mSv/MBq), and liver (0.0429 mSv/MBq). Lung tissue exhibited low uptake of ^{18}F-PEG$_6$-IPQA due to the low affinity of this radiotracer to wild-type epidermal growth factor receptor kinase. The effective dose was 0.0165 mSv/MBq. No evidence of acute cardiotoxicity or of acute or delayed systemic toxicity was observed. On the basis of our estimates, diagnostic dosages of ^{18}F-PEG$_6$-IPQA up to 128 MBq (3.47 mCi) per injection should be safe for administration in the initial cohort of human patients in phase I clinical PET studies. **Conclusion:** The whole-body and individual organ radiation dosimetry characteristics and pharmacologic safety of diagnostic dosages of ^{18}F-PEG$_6$-IPQA in nonhuman primates indicate that this radiotracer should be acceptable for PET/CT studies in human patients.

Key Words: epidermal growth factor receptor; PET; ^{18}F-PEG$_6$-IPQA; radiation dosimetry; nonhuman primate

J Nucl Med 2011; 52:934–941
DOI: 10.2967/jnumed.110.086777

Over the past decade, the oncogenic role of the epidermal growth factor receptor (EGFR) has been increasingly characterized because of improved understanding of the mechanisms of receptor activation, the finding of somatic mutations of this receptor, mutations in components of the signaling pathway of the receptor, and the clinical success of anti-EGFR therapies for cancer patients (*1*). Therapeutic responses to anti-EGFR agents differ in patients and are sometimes contradictory, depending on the tumor type and clinical setting. Emerging data suggest that certain activating mutations in the EGFR kinase domain in patients with non–small cell lung carcinomas (NSCLC) are more frequent in nonsmokers, women, and those with adenocarcinoma histology or who are of Asian ethnicity (*2–5*) and are associated with responsiveness to gefitinib and other EGFR inhibitors. EGFR overexpression identified using immunohistochemistry correlates with EGFR amplification detected by fluorescence in situ hybridization but not necessarily with EGFR mutations or response to therapy with EGFR kinase inhibitors (*6*).

Without accurate in vivo measurements of EGFR expression and signaling activity in human tumors, it is impossible to predict the responsiveness of tumors to EGFR kinase inhibitors or to determine whether a poor tumor response to an EGFR-targeted drug results from the lack of specific

Received Dec. 16, 2010; revision accepted Jan. 31, 2011.
For correspondence or reprints contact either of the following: Juri G. Gelovani, Department of Experimental Diagnostic Imaging, University of Texas M.D. Anderson Cancer Center, 1515 Holcombe Blvd., Houston, TX 77030.
E-mail: jgelovani@mdanderson.org
Mei Tian, Department of Experimental Diagnostic Imaging, University of Texas M.D. Anderson Cancer Center, 1515 Holcombe Blvd., Houston, TX 77030.
E-mail: mei.tian@mdanderson.org

activating mutations, the absence of a survival function of EGFR, insufficient long-term occupancy of the receptor by reversible inhibitors, or a high rate of receptor regeneration when using irreversible inhibitors. Although invasive tissue sampling can provide spatially limited, temporally static information about the expression or activity of EGFR at the kinase level, multiple sampling of heterogeneous tumor tissue and repeated biopsies are almost always infeasible. Consequently, interest in the use of EGFR tyrosine kinase inhibitors as radiotracers for noninvasive molecular imaging with PET of tumors that overexpress EGFR, especially tumors expressing constitutively active EGFR mutants, has been growing over the past several years (*7*), because noninvasive PET may facilitate repetitive quantitative assessment of the magnitude and heterogeneity of EGFR expression and activity at the kinase level in tumors in individual patients.

Several radiolabeled small-molecule agents for PET of EGFR expression at the kinase level have been reported to date (summarized in the supplemental materials, available online only at http://jnm.snmjournals.org). Recently, we reported on successful development and evaluation of a new radiotracer 4-[(3-iodophenyl)amino]-7-(2-[2-{2-(2-[2-{2-(^{18}F-fluoroethoxy)-ethoxy}-ethoxy]-ethoxy)-ethoxy}-ethoxy]-quinazoline-6-yl-acrylamide) (^{18}F-PEG$_6$-IPQA) (*8*). PET/CT studies in mice bearing human NSCLC xenografts demonstrated that ^{18}F-PEG$_6$-IPQA could distinguish tumors expressing constitutively active mutant L858R EGFR that are responsive to therapy with EGFR kinase inhibitors from tumors expressing wild-type EGFR or L858R/T790M dual-mutant EGFR that are resistant to such therapy (*9*). Therefore, we suggest that high levels of ^{18}F-PEG$_6$-IPQA accumulation in NSCLC lesions should predict favorable responses to therapy with EGFR kinase inhibitors. Also, repetitive PET/CT with ^{18}F-PEG$_6$-IPQA could potentially be used in patients for noninvasive monitoring of pharmacodynamics of EGFR kinase inhibitors at the target level.

For the preparation of an investigational new drug application for clinical phase I imaging studies, the Food and Drug Administration regulatory guidelines require the assessment of pharmacologic and radiation safety of novel radiolabeled imaging agents. Nonhuman primates (i.e., rhesus macaques) are genetically close to humans and have similar anatomy, physiology, and metabolism. They therefore provide an ideal model for the evaluation of pharmacokinetics, metabolism, radiation dosimetry, and pharmacologic safety of novel radiotracers (*10*).

Here, we report the results of PET/CT studies in nonhuman primates aimed at determining the pharmacokinetics, biodistribution, metabolism, radiation dosimetry, and pharmacologic safety of diagnostic doses of ^{18}F-PEG$_6$-IPQA and at extrapolating to radiation dose estimates for humans.

MATERIALS AND METHODS

^{18}F-PEG$_6$-IPQA Preparation

^{18}F-PEG$_6$-IPQA was synthesized as described previously (*8*). ^{18}F-PEG$_6$-IPQA was purified using high-performance liquid chromatography (HPLC) (>97% pure). The mass of nonradioactive F-PEG$_6$-IPQA was 0.91 ± 0.41 μg per 1 mCi (37 mBq), and the specific activity of ^{18}F-PEG$_6$-IPQA was 33.67 ± 12.95 GBq/μmol (0.91 ± 0.35 Ci/μmol), based on 17 radiosynthesis batches.

Experimental Animals

Six rhesus macaques (3 female and 3 male; body weight, 6–11 kg) were included in this study. All experiments were performed following institutional guidelines for conducting experiments in nonhuman primates under an Institutional Animal Care and Use Committee–approved research protocol. Before imaging, the animals were kept fasting overnight but had free access to water. To facilitate intubation, the animals were premedicated with atropine sulfate (0.04 mg/kg) intramuscularly and anesthetized with ketamine (10–15 mg/kg) intramuscularly, followed by inhalation anesthesia with isoflurane 1%–3% and oxygen delivered by an Excel 210 SE gas anesthesia system (Ohmeda Inc.). After intubation and stabilization of vital signs under anesthesia, the animals were cannulated in both saphenous veins: one cannula was used for injection of ^{18}F-PEG$_6$-IPQA, and the other was used for repetitive blood sampling during imaging. Also, the urinary bladder was catheterized and the catheter clamped to collect radioactive urine after the PET/CT scan. Body temperature was maintained at 37°C ± 0.8°C using an air-circulating heating device (model 505; Arizant Healthcare Inc.). The electrocardiogram, blood pressure, pulse oxymetry, and respiration rates were monitored using a Solar 8000 system (Marquette Medical Systems, Inc.) throughout the imaging study.

PET/CT Study

PET/CT studies were performed using a Discovery ST8 PET/CT system (GE Healthcare). The CT component of the study consisted of a helical scan covering the head to the mid thighs (120 kVp, 300 mA, 0.5-s rotation; table speed, 13.5 mm/rotation) with no contrast enhancement. Axial CT images were reconstructed with a slice thickness of 3.75 mm. A dynamic PET scan was then acquired starting with the onset of the ^{18}F-PEG$_6$-IPQA injection, which was administered intravenously. Each animal received a dosage of 141 ± 59.2 MBq (3.8 ± 1.6 mCi) of ^{18}F-PEG$_6$-IPQA in a volume of 5 mL of normal saline as a continuous infusion over 1 min using a digital dual-syringe infusion pump (model 33; Harvard Apparatus). Simultaneously with the ^{18}F-PEG$_6$-IPQA infusion, 15 mL of saline was infused using a second syringe through the same catheter port; this infusion of saline continued for another 4 min after the end of the ^{18}F-PEG$_6$-IPQA injection to steadily flush the infusion line (Supplemental Fig. 1). Such a dual-infusion approach was used to prevent spikes in radioactivity concentration in the blood, which usually occur because of a bolus flush after the radiotracer injection.

Dynamic PET covering the thoracoabdominal area was performed for the first 30 min, followed by 4 whole-body static images from the mid femoral position to the head at 60, 90, 120, and 180 min after the injection of ^{18}F-PEG$_6$-IPQA. The whole-body static PET images were acquired in 3-dimensional mode for 3 min per bed position. Also, a low-dose, unenhanced CT scan was obtained immediately after the dynamic PET scan and at the end of the last PET scan to ensure accurate coregistration of PET and CT images (Supplemental Fig. 2).

PET images were reconstructed using standard vendor-provided reconstruction algorithms that incorporated ordered-subset expectation maximization and corrected for attenuation using data from the CT component of the examination; the emission data were

corrected for scatter, random events, and dead-time losses using the PET/CT scanner's standard algorithms. The dose calibrator (CRC-15R; Capintec) was cross-calibrated with the PET/CT instrument to ensure the quantitative accuracy of the PET data.

Image Analysis

Regional dynamic and whole-body reconstructed PET/CT data were stored in the Digital Imaging and Communications in Medicine 3.0, part 10, file format and transferred to a HERMES Workstation (version 2.2; Nuclear Diagnostics AB). Three-dimensional volumes of interest (VOIs) of identifiable source organs were constructed on the CT images, and their positions were verified on the corresponding PET images to include all organ activity. These VOIs were then used for PET image analysis. The identifiable source organs analyzed were the heart, liver, gallbladder, kidneys, urinary bladder, small and large intestines, brain, and whole body. Three-dimensional VOI definitions were used to visually inspect for misregistration due to motion between sequential scans in the same segment. Residual errors were manually corrected by redefining the VOIs when necessary; this was necessary only for the gallbladder and urinary bladder, which showed gradual accumulation of radioactivity as well as enlargement over the course of the PET scan.

Residence Time and Absorbed Radiation Dose Calculations

Individual organ and whole-body time–activity curves were fitted to a monoexponential or biexponential function using SigmaPlot software (version 11; Systat Software). If the data were not well approximated by exponentials, they were fitted by trapezoidal approximations of the measured data followed by exponential decay with the physical half-life from the last measured radioactivity concentration. The residence time for the exponential fits was calculated by dividing the fractional uptake by the decay constant. For biexponential fits, the residence time was the sum of this ratio for each term. For trapezoidal approximations of ^{18}F-PEG$_6$-IPQA, the area under the curve was calculated and divided by the administered activity of ^{18}F-PEG$_6$-IPQA to yield the residence time. The residence time for the blood was calculated using the time–activity curve of the drawn blood samples, assuming that 8% of the animal's mass was blood.

Because the animals were catheterized and could not void their bladders during the PET/CT scans, radioactive urine accumulated in their bladders. For each animal, we estimated the fraction in the bladder from the activity in a later PET image divided by the decayed administered activity and the biologic half-life by a fit to a single exponential increase-to-maximum fit to the decay-corrected bladder time–activity curve. These parameters were used to estimate the residence time for ^{18}F-PEG$_6$-IPQA in the bladder using the dynamic bladder model in the OLINDA/EXM 1.1 software program (Vanderbilt University) (*11*), with the assumption of a 2-h voiding interval.

The residence times, including those in the blood, were humanized using the mass of each organ estimated using the CT scans of the nonhuman primates and the mass of each organ in the MIRD 70-kg standard man model as inputs to Equation 8 according to the report by Macey (*12*). The blood residence time was then apportioned among the organs according to their blood volume fractions tabulated in the International Commission on Radiological Protection publication 53 (*13*). The human dosimetry of ^{18}F-PEG$_6$-IPQA was then estimated using these humanized residence times and the adult male and adult female models in the OLINDA/EXM software program.

Blood Sampling and Analyses

Immediately before ^{18}F-PEG$_6$-IPQA injection in each animal, a 0.5-mL blood sample was drawn to measure the hematocrit and blood gases with an i-STAT portable analyzer (Abbott Point of Care). ^{18}F-PEG$_6$-IPQA was injected only if the hematologic and blood chemical parameters in the blood sample were all within the reference ranges. Subsequently, 0.5-mL venous blood samples were obtained via the catheterized vein at 10, 20, 40, 60, and 90 s and 2, 3, 5, 8, 16, 32, 60, 90, 120, and 180 min after ^{18}F-PEG$_6$-IPQA injection. At the end of each PET/CT session, an additional blood sample (0.5 mL) was obtained and analyzed using an i-STAT portable analyzer to determine potential acute toxic side effects from the diagnostic dose of ^{18}F-PEG$_6$-IPQA.

The blood and plasma were assayed for radioactivity concentration using a γ-counter (Cobra Quantum; PerkinElmer). A portion of each plasma sample was extracted with acetonitrile and subjected to radio-HPLC analysis using an analytic HPLC system (model 1100; Agilent Technologies) equipped with a PET metabolite radiodetector (Flow-Count; Bioscan). The analysis was performed using a ZORBAX Eclipse XDB-C8 column (4.6 × 150 mm; Agilent Technologies) with a mobile phase consisting of acetonitrile/10 mM ammonium acetate buffer (47/53 ratio; pH 5.5) at a 1 mL/min flow rate. Under these conditions, the retention time was 7.2 min for ^{18}F-PEG$_6$-IPQA, whereas the major radioactive catabolite, ^{18}F-PEG$_6$, eluted at 1.7 min, as determined using ^{18}F-PEG$_6$, an authentic standard. The fraction of ^{18}F-PEG$_6$-IPQA versus the radiometabolite (^{18}F-PEG$_6$) fraction for each sample was determined on the basis of their respective radioactive peak areas. The total radioactivity in plasma was expressed as percentage injected dose per milliliter and plotted over time after injection of ^{18}F-PEG$_6$-IPQA. Also, the percentage injected dose per milliliter of intact ^{18}F-PEG$_6$-IPQA and ^{18}F-PEG$_6$ catabolite was calculated from the radio-HPLC results and plotted over time after injection of ^{18}F-PEG$_6$-IPQA to generate the corresponding time–activity curves. The percentage of ^{18}F-PEG$_6$-IPQA bound to red blood cells (RBCs) versus blood plasma was determined by mixing ^{18}F-PEG$_6$-IPQA with heparinized blood and incubating for 15 min at 37°C, separating RBC and plasma by centrifugation at 3,000 rpm for 5 min and measuring the radioactivity concentration in plasma and the RBC pellet.

Urine Analysis

Whole urine was sampled from each animal at the end of PET via a Foley catheter. The total radioactivity of each sample was measured using a γ-counter. Samples were subjected to the same radio-HPLC analysis as for the blood samples.

Assessment of Acute Toxicity of ^{18}F-PEG$_6$-IPQA

The vital signs, electrocardiogram results, blood pressure, pulse oxymetry, and respiration rate of experimental animals were monitored throughout the animal preparation and imaging session. Detailed physical examinations of the monkeys were performed by experienced veterinarians immediately before ^{18}F-PEG$_6$-IPQA PET/CT and on days 3 and 14 after ^{18}F-PEG$_6$-IPQA injection. Additional blood samples (5–10 mL) were drawn from each animal before and immediately after the imaging study and at 3 and 14 d after the PET study for extensive hematologic and toxicologic analyses (including liver enzymes, creatine, and nitrogen) performed by an accredited veterinary clinical laboratory.

TABLE 1
Administered Doses of ^{18}F-PEG$_6$-IPQA in Study Animals

Characteristic	All	Female	Male
Age (y)	12.3 ± 5.4	14.7 ± 7.2	10 ± 1.7
Body weight (kg)	8.5 ± 2.8	6.3 ± 0.6	10.7 ± 2.3
Administered activity (MBq)	141 ± 59.2	148 ± 213	133 ± 33.3
Administered activity/kg (MBq/kg)	18.5 ± 11.1	22.2 ± 14.8	14.8 ± 3.7

Data are presented as mean ± SD.

RESULTS

The mean ages, body weights of the experimental animals, and injected ^{18}F-PEG$_6$-IPQA doses are listed in Table 1. All monitored clinical parameters, including heart and respiration rates, body temperature, blood pressure, electrocardiogram results, and saturation of peripheral oxygen (SPO_2), were within the reference ranges throughout the experiments. During and after PET/CT and over the 14 d follow-up period, none of the animals developed any adverse events. There were no significant differences in hematologic and biochemical parameters measured before and immediately after the study or 3 and 14 d after ^{18}F-PEG$_6$-IPQA administration, except for a transient increase in alanine aminotransferase (ALT) on day 3, which returned to baseline level by day 14 after the PET/CT study (Supplemental Table 1).

Dynamic PET revealed the pattern and kinetics of ^{18}F-PEG$_6$-IPQA distribution and clearance at 180 min after intravenous administration (Fig. 1). The ^{18}F-PEG$_6$-IPQA–derived radioactivity peaked in the heart and kidneys within 1 min after initiation of administration and then started to accumulate in the liver and gallbladder. By 30–60 min after injection, organs involved in the hepatobiliary and renal clearance pathways dominated the whole-body distribution of ^{18}F-PEG$_6$-IPQA, with the highest radioactivity concentration in the gallbladder, parts of the small and upper large intestines, the kidney, and the urinary bladder. Individual source organ time–activity curves for ^{18}F-PEG$_6$-IPQA–derived radioactivity are shown in Figure 2. The steady-bolus injection method allowed for reliable identification of the peak of total radioactivity concentration and of the concentration in blood plasma of intact ^{18}F-PEG$_6$-IPQA and ^{18}F-PEG$_6$ catabolite (Fig. 3). ^{18}F-PEG$_6$-IPQA binding to RBCs was negligible; 96% ± 1% of radioactivity was recovered in blood plasma. The total blood radioactivity concentration peaked at 2.6 min after the initiation of ^{18}F-PEG$_6$-IPQA administration and gradually decreased thereafter, conforming to biexponential kinetics, with average half-lives of 2.0 ± 0.1 and 20.3 ± 1.6 min for the fast and slow components, respectively. The radioactivity concentration from intact ^{18}F-PEG$_6$-IPQA also peaked at 2.6 min after the initiation of ^{18}F-PEG$_6$-IPQA administration and gradually decreased thereafter, conforming to biexponential kinetics, with average half-lives of 1.6 ± 0.1 and 12.6 ± 1.2 min for the fast and slow components, respectively. The major radioactive catabolite of ^{18}F-PEG$_6$-IPQA in blood was identified as ^{18}F-PEG$_6$, the concentration of which in blood peaked at 5 min after intravenous administration of ^{18}F-PEG$_6$-IPQA. The clearance of ^{18}F-PEG$_6$ from blood followed biexponential kinetics, with half-lives of 16.1 ± 1.3 min and 74.6 ± 2.2 min for the fast and slow components, respectively. Three hours after ^{18}F-PEG$_6$-IPQA administration, the predominant fraction of urine radioactivity (>95%) was due to ^{18}F-PEG$_6$ and products derived from further breakdown of ^{18}F-PEG$_6$, such as ^{18}F-fluoroacetate (3%–5%), with only minute amounts of ^{18}F-fluoride.

To estimate the maximum dosage of ^{18}F-PEG$_6$-IPQA that could be safely administered to human patients, individual

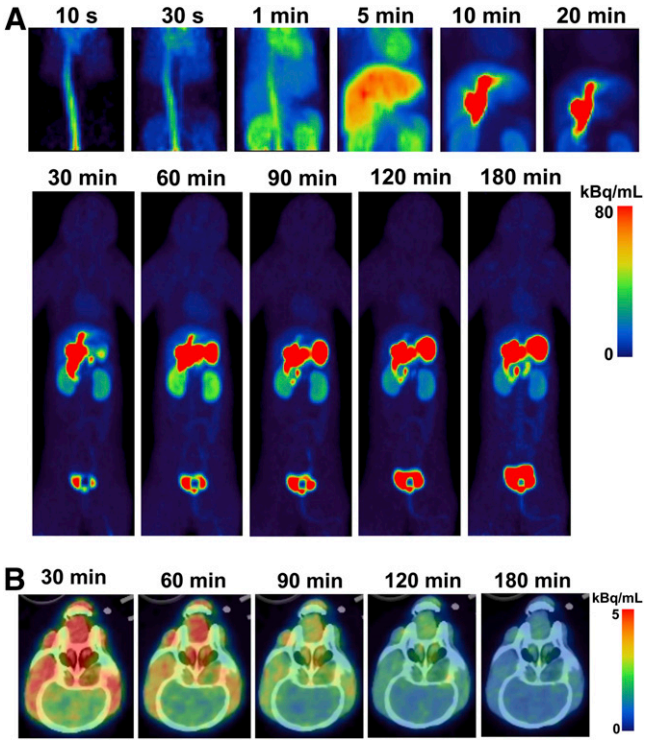

FIGURE 1. PET images of distribution of ^{18}F-PEG$_6$-IPQA radioactivity in representative animal at different time points after intravenous injection. (A) Maximum-intensity-projection PET images of whole body. (B) Representative axial PET/CT images of head, demonstrating ability of ^{18}F-PEG$_6$-IPQA to cross normal blood–brain barrier.

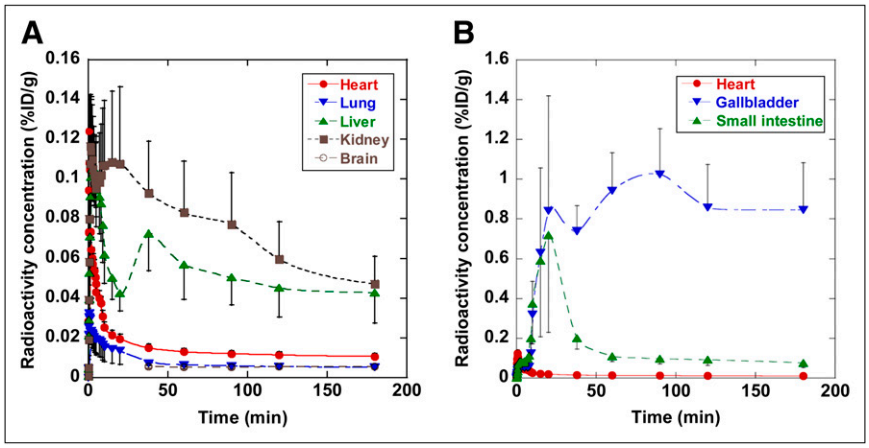

FIGURE 2. Time–activity curves of ^{18}F-PEG$_6$-IPQA in key organs of rhesus macaques: heart, lung, liver, kidney, and brain (A) and heart, gallbladder, and small intestine (B). Plots A and B have different ranges of radioactivity concentrations. Values are means, and bars are SEs.

organ-absorbed radiation doses were calculated using the corresponding organ radioactivity residence times, τ (Table 2). The maximum possible τ was $T_{physical}/\ln(2) = 1.443 \times 109.8 = 158$ min (2.64 h). The fact that the mean sum of the residence times was close to the maximum possible τ indicates that all of the administered activity was accounted for. Estimates of the human individual organ radiation-absorbed doses per unit administered activity of ^{18}F-PEG$_6$-IPQA are presented in Table 3.

The gallbladder received the highest absorbed dose (0.394 mSv/MBq), making it the limiting organ. The relatively high dose to the gallbladder is due to the rapid extraction of ^{18}F-PEG$_6$-IPQA from the circulation by the liver and thus the excretion of a large fraction of injected radioactivity into the gallbladder. The other key organs with high absorbed radiation doses were the kidneys (0.0830 mSv/MBq), upper large intestine wall (0.0267 mSv/MBq), small intestine (0.0816 mSv/MBq), and liver (0.0429 mSv/MBq). On the other hand, the skin, breast, brain, thymus, thyroid, and testes received much lower radiation doses. The effective dose was 0.0165 mSv/MBq. Therefore, administration of diagnostic dosages of ^{18}F-PEG$_6$-IPQA up to 128 mBq (3.47 mCi) per intravenous injection should be safe for the initial cohort of patients participating in a phase I clinical study.

DISCUSSION

In this study, the pharmacokinetics, biodistribution, metabolism, and radiation dosimetry of the new radiotracer ^{18}F-PEG$_6$-IPQA was assessed in healthy rhesus macaques using dynamic PET and serial blood sampling.

After intravenous administration, ^{18}F-PEG$_6$-IPQA did not cause acute or delayed toxicity up to 14 d, except for a transient increase of ALT 3 d after the study, which decreased back to baseline level by 14 d after the study. This transient increase in ALT is most likely due to ketamine and isoflurane anesthesia (which are known to cause transient upregulation of liver transaminases lasting for several days after anesthesia) lasting for more than 4 h (including time required for the animal preparation and transportation to and from the imaging suite) (*14,15*).

The lack of toxicity or any detectable pharmacologic effects from the diagnostic doses of ^{18}F-PEG$_6$-IPQA was expected, because the total amount of nonradiolabeled, pharmacologically active F-PEG$_6$-IPQA administered to each animal was in the range of 3–5 μg. This mass dose is about 50,000- to 80,000-fold less than the average single therapeutic dose of gefitinib (250 mg, by mouth) and 30,000- to 50,000-fold less than that of erlotinib (150 mg, by mouth),

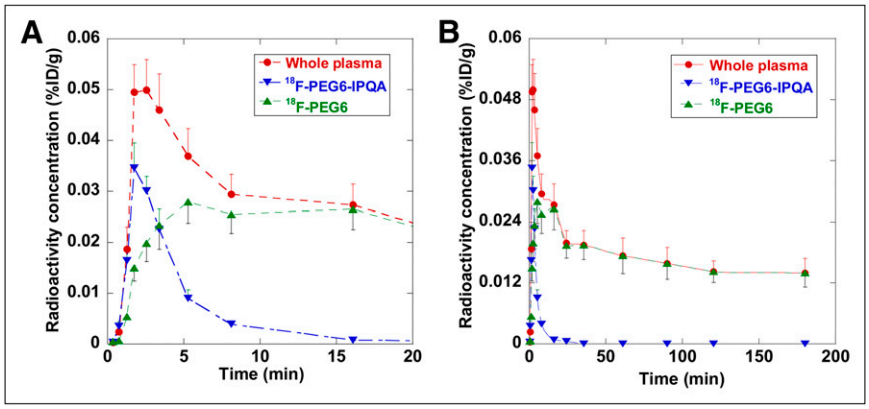

FIGURE 3. Time–activity curves of total radioactivity in blood plasma, intact ^{18}F-PEG$_6$-IPQA, and ^{18}F-PEG$_6$ (major metabolite) from 0 to 20 min (A) and from 0 to 180 min (B) after intravenous injection of ^{18}F-PEG$_6$ IPQA in rhesus macaques. Values are means, and bars are SEs.

TABLE 2
Humanized ^{18}F-PEG$_6$-IPQA Residence Times (Hours) in Nonhuman Primates

Organ	Female	Male	All
Blood	0.48 ± 0.25	0.33 ± 0.13	0.41 ± 0.20
Brain	0.024 ± 0.006	0.023 ± 0.005	0.024 ± 0.005
Gallbladder	0.32 ± 0.18	0.15 ± 0.09	0.24 ± 0.16
Heart	0.011 ± 0.003	0.010 ± 0.002	0.011 ± 0.002
Kidneys	0.17 ± 0.14	0.061 ± 0.037	0.12 ± 0.11
Liver	0.29 ± 0.11	0.25 ± 0.16	0.27 ± 0.13
Lungs*	0.049 ± 0.025	0.034 ± 0.013	0.041 ± 0.020
Red marrow*	0.018 ± 0.009	0.012 ± 0.005	0.015 ± 0.007
Small intestine	0.24 ± 0.16	0.35 ± 0.19	0.29 ± 0.17
Remainder of body	1.2 ± 0.32	1.68 ± 0.11	1.46 ± 0.32
Urinary bladder contents			0.024 ± 0.089
Total residence time	2.45 ± 0.19	2.75 ± 0.12	2.64 ± 0.22

*Lung and red marrow times are derived from blood residence time.
Data are presented as mean ± SD.

which is administered once daily for 4 wk for therapy of patients with NSCLC (*16–19*).

From the dynamic PET images, it is evident that ^{18}F-PEG$_6$-IPQA accumulates only transiently in the organs of the hepatobiliary and renal systems, which contribute to clearance of ^{18}F-PEG$_6$-IPQA from the circulation. Initially, the intact ^{18}F-PEG$_6$-IPQA is absorbed by the liver because of its relatively high lipophilicity (LogD = 1.44). Then, the ^{18}F-PEG$_6$-IPQA–derived radioactivity is excreted into the gallbladder and later evacuated into the small intestine. This partially explains the reason for higher radiation doses estimated for the gallbladder, upper large intestine wall,

TABLE 3
Radiation-Absorbed Dose Estimates (mSv/MBq) for ^{18}F-PEG$_6$-IPQA

Target organ	Adult female model using female residence times	Adult male model using male residence times	Adult male model using average residence times
Adrenals	2.03E−02	1.45E−02	1.55E−02
Brain	6.36E−03	5.70E−03	5.64E−03
Breasts	7.96E−03	7.74E−03	7.12E−03
Gallbladder wall	5.79E−01	2.53E−01	3.94E−01
Heart wall	1.48E−02	1.28E−02	1.25E−02
Kidneys	1.23E−01	4.67E−02	8.30E−02
Liver	6.03E−02	3.86E−02	4.29E−02
Lower large intestine wall	1.48E−02	1.55E−02	1.45E−02
Lungs	1.76E−02	1.16E−02	1.27E−02
Muscle	1.07E−02	1.03E−02	9.73E−03
Osteogenic cells	1.52E−02	1.45E−02	1.34E−02
Ovaries	1.79E−02		
Pancreas	2.21E−02	1.64E−02	1.78E−02
Red marrow	1.20E−02	1.13E−02	1.12E−02
Skin	7.17E−03	7.32E−03	6.70E−03
Small intestine	7.14E−02	8.14E−02	8.16E−02
Spleen	1.50E−02	1.19E−02	1.21E−02
Stomach wall	1.59E−02	1.35E−02	1.34E−02
Testes		8.80E−03	7.78E−03
Thymus	9.43E−03	9.19E−03	8.34E−03
Thyroid	7.56E−03	8.72E−03	7.68E−03
Upper large intestine wall	2.87E−02	2.58E−02	2.67E−02
Urinary bladder wall	2.50E−02	2.25E−02	2.16E−02
Uterus	1.71E−02	1.82E−02	1.73E−02
Total body	1.33E−02	1.20E−02	1.17E−02
Effective dose equivalent	6.16E−02	3.60E−02	4.67E−02
Effective dose	1.97E−02	1.57E−02	1.65E−02

small intestine, and liver. At this time, we do not know exactly what ^{18}F-labeled metabolites are excreted into the gallbladder. However, after the degradation of ^{18}F-PEG$_6$-IPQA, the major radioactive catabolite, ^{18}F-PEG$_6$, is eliminated from the circulation predominantly by the kidneys into the bladder, which are also among the critical organs. Little ^{18}F-fluoride was found in the blood and urine, as evidenced by the absence of radioactivity accumulation in the skeletal structures on PET/CT images. The background radioactivity in other organs, including the heart, was very low to negligible and decreased further with time. Thus, current radiation dosimetry estimates for ^{18}F-PEG$_6$-IPQA derived from nonhuman primates indicate acceptable radiation-absorbed doses to the critical organs (liver, gallbladder, intestine, kidney, and bladder) and even lower radiation-absorbed doses to radiation-sensitive organs in human patients. It should be possible to shorten the residence time and decrease the absorbed dose to the gallbladder by administering cholecystokinin or sincalide (*20–22*), which should allow for the safe administration of higher or repetitive dosages of ^{18}F-PEG$_6$-IPQA without exceeding the 50 mSv per organ per year limit for compounds that might be "generally recognized as safe" according to the Food and Drug Administration regulations (title 21 of *Code of Federal Regulations* part 361.1). On the basis of our estimates, diagnostic dosages of ^{18}F-PEG$_6$-IPQA up to 128 mBq (3.47 mCi) per injection should be safe for administration in the initial cohort of human patients in phase I clinical PET studies.

Recently, the biodistribution and radiation dosimetry of the ^{11}C-labeled EGFR kinase inhibitor, ^{11}C-PD153035, was assessed with PET in 12 healthy human volunteers (*23*). In that study, after administration of 329.3 ± 77.8 MBq of ^{11}C-PD153035, the highest radiation-absorbed doses were observed in the urinary bladder, gallbladder, liver, small intestine, and kidney, as is consistent with our current study. However, direct comparison of results obtained in the ^{11}C-PD153035 study with our current study is not feasible because neither blood sampling nor radioactive decay correction was performed in the ^{11}C-PD153035 study.

^{18}F-PEG$_6$-IPQA accumulation was low in tissues known to express higher levels of EGFR, such as lung parenchyma, bronchi, and intestine. The lack of ^{18}F-PEG$_6$-IPQA accumulation in these organs can be explained by the high specificity of the tracer for irreversible binding to the active mutant L858R EGFR and its significantly lower affinity to the wild-type EGFR, as was demonstrated by us previously (*9*). Compared with ^{18}F-PEG$_6$-IPQA in rhesus macaques, other radiolabeled EGFR kinase inhibitors, such as ^{18}F-gefitinib, demonstrated similar biodistribution in vervet monkeys (*24*), except for higher retention in the lungs. Similarly, ^{11}C-PD153035 (*23*) exhibited higher retention in the lungs of human patients than did ^{18}F-PEG$_6$-IPQA. These differences are probably due to the higher affinity of ^{18}F-gefitinib and ^{11}C-PD153035 to wild-type EGFR kinase, as compared with ^{18}F-PEG$_6$-IPQA, which is more specific to mutant L858R EGFR kinase (*8,9*).

On the basis of the observed pattern of ^{18}F-PEG$_6$-IPQA biodistribution and radiation dosimetry estimates in nonhuman primates, we suggest that imaging of the L858R mutant EGFR expression in NSCLC with ^{18}F-PEG$_6$-IPQA should be feasible in human patients in the chest area and remote sites, except for liver metastases. PET could be initiated at 1 h after intravenous injection of ^{18}F-PEG$_6$-IPQA, to allow for the background activity in the liver to decline sufficiently and enable effective imaging of the lower thoracic region. Because the time–activity curves of ^{18}F-PEG$_6$-IPQA in the brain and muscle were similar, it is likely that this radiotracer can cross the normal blood–brain barrier by nonfacilitated diffusion and equilibrate between blood and brain tissue, which is most likely due to its fairly high lipophilicity. Consequently, ^{18}F-PEG$_6$-IPQA could also be evaluated for early detection of metastases of NSCLC to the brain.

Two relatively novel techniques were implemented in the current study. One technique used a dual-syringe injection pump–based steady-bolus infusion of the radiotracer, preventing the development of spikes of radioactivity concentration in the blood, which usually occurs because of a flush bolus (of saline) after radiotracer injection. The other technique used corresponding CT-based 3-dimensional VOIs to calculate the volume of organs and then verified them on the corresponding PET emission images to include all organ activity. Three-dimensional VOIs were used to visually inspect for movement artifacts between sequential scans in the same segment. Residual errors were manually corrected by redefining VOIs for the gallbladder and urinary bladder, which showed dynamic volume and radioactive concentration changes during the 180-min course of the PET study. Using these techniques, we achieved a mean total residence time that was similar to the maximum possible τ, whereas the SD of means of pharmacokinetic parameters for ^{18}F-PEG$_6$-IPQA and ^{18}F-PEG$_6$ in blood varied less than 5%, demonstrating high reproducibility.

The current study, however, has some limitations. The pharmacokinetics, biodistribution, and metabolism of ^{18}F-PEG$_6$-IPQA were studied in animals under general anesthesia, which could interfere with hemodynamics in certain organs and thus influence metabolism. Although blood flow to the liver is altered less by isoflurane than by other anesthesia methods, renal blood flow and urine volume are decreased by isoflurane (*25*). In previous PET studies of animals and humans, general anesthesia caused significant reduction in brain glucose metabolism, suggesting that conscious monkeys should be a better model for the future studies (*26,27*). General anesthesia could also affect the metabolism of ^{18}F-PEG$_6$-IPQA.

CONCLUSION

The pharmacokinetics, metabolism, biodistribution, and radiation dosimetry characteristics of ^{18}F-PEG$_6$-IPQA studied in nonhuman primates indicate that diagnostic dosages of this radiotracer should be safe for PET in human

patients. The highest radiation dose is delivered to the gallbladder. The dose estimation and radiation doses delivered to other radiosensitive organs must be considered when evaluating the dosimetry of multiple administrations of ^{18}F-PEG$_6$-IPQA to human patients.

DISCLOSURE STATEMENT

The costs of publication of this article were defrayed in part by the payment of page charges. Therefore, and solely to indicate this fact, this article is hereby marked "advertisement" in accordance with 18 USC section 1734.

ACKNOWLEDGMENTS

We thank Dana Toomey, Julie Basham, Deborah Petit, Alfredo Santiago, and Jennifer Miller for their excellent veterinary technical support and Nancy Swanston for help with PET/CT studies. We thank Karen Yoas for help in coordinating this study. This work was supported by the following grants: W81XWH-05-2-0027, 5U24CA126577, and NIH-NCI CA-016672 (Cancer Center Support grant), and the H.H. Laughery philanthropic gift.

REFERENCES

1. Scaltriti M, Baselga J. The epidermal growth factor receptor pathway: a model for targeted therapy. *Clin Cancer Res.* 2006;12:5268–5272.
2. Fukuoka M, Yano S, Giaccone G, et al. Multi-institutional randomized phase II trial of gefitinib for previously treated patients with advanced non-small-cell lung cancer (The IDEAL 1 Trial). *J Clin Oncol.* 2003;21:2237–2246.
3. Shepherd FA, Tsao MS. Unraveling the mystery of prognostic and predictive factors in epidermal growth factor receptor therapy. *J Clin Oncol.* 2006;24:1219–1220; author reply 1220-1211.
4. Mu XL, Li LY, Zhang XT, Wang SL, Wang MZ. Evaluation of safety and efficacy of gefitinib ('iressa', zd1839) as monotherapy in a series of Chinese patients with advanced non-small-cell lung cancer: experience from a compassionate-use programme. *BMC Cancer.* 2004;4:51.
5. Tsao MS, Sakurada A, Cutz JC, et al. Erlotinib in lung cancer: molecular and clinical predictors of outcome. *N Engl J Med.* 2005;353:133–144.
6. Chintala L, Kurzrock R. Epidermal growth factor receptor mutation and diverse tumors: case report and concise literature review. *Mol Oncol.* 2010;4:306–308.
7. Mishani E, Abourbeh G, Eiblmaier M, Anderson CJ. Imaging of EGFR and EGFR tyrosine kinase overexpression in tumors by nuclear medicine modalities. *Curr Pharm Des.* 2008;14:2983–2998.
8. Pal ABJ, Mukhopadhyay U, Ogawa K, et al. Radiosynthesis and initial in vitro evaluation of [^{18}F]-PEG6-IPQA: a novel PET radiotracer for imaging EGFR expression-activity in lung carcinomas. *Mol Imaging Biol*. September 22, 2010 [Epub ahead of print].
9. Yeh H-H, Ogawa K, Balatoni J, et al. Molecular imaging of active mutant L858R EGFR in non small cell lung carcinoma using [^{18}F]-PEG6-IPQA and PET/CT. *Proc Natl Acad Sci USA*. 2011;108:1603–1608.
10. Tian M. Welch MJ. Translational molecular imaging in drug development: current status and challenges. *Curr Med Imaging Rev.* 2010;6:51–55.
11. Stabin MG, Sparks RB, Crowe E. OLINDA/EXM: the second-generation personal computer software for internal dose assessment in nuclear medicine. *J Nucl Med.* 2005;46:1023–1027.
12. Macey DJ, Williams LE, Breitz HB, Liu A, Johnson TK, Zanzonico PB. American Association of Physicists in Medicine (AAPM) Report 71. *A Primer for Radioimmunotherapy and Radionuclide Therapy.* Available at: http://www.aapm.org/pubs/reports/rpt_71.pdf. Accessed April 8, 2011.
13. Radiation dose to patients from radiopharmaceuticals (addendum 2 to ICRP publication 53). *Ann ICRP.* 1998;28:1–126.
14. Nishiyama T, Yokoyama T, Hanaoka K. Effects of sevoflurane and isoflurane anesthesia on arterial ketone body ratio and liver function. *Acta Anaesthesiol Scand.* 1999;43:347–351.
15. Woodward RA, Weld KP. A comparison of ketamine, ketamine-acepromazine, and tiletamine-zolazepam on various hematologic parameters in rhesus monkeys (Macaca mulatta). *Contemporary Top Lab Anim Sci.* 1997;36:55–57.
16. Kris MG, Natale RB, Herbst RS, et al. Efficacy of gefitinib, an inhibitor of the epidermal growth factor receptor tyrosine kinase, in symptomatic patients with non-small cell lung cancer: a randomized trial. *JAMA.* 2003;290:2149–2158.
17. Iressa [package insert]. Available at: http://www1.astrazeneca-us.com/pi/iressa.pdf. Accessed April 8, 2011.
18. Shepherd FA, Rodrigues Pereira J, Ciuleanu T, et al. Erlotinib in previously treated non-small-cell lung cancer. *N Engl J Med.* 2005;353:123–132.
19. Tarceva [package insert]. Available at: http://www.osip.com/pdf/Tarceva_PI_042010.pdf. Accessed April 8, 2011.
20. Ziessman HA. Cholecystokinin cholescintigraphy: clinical indications and proper methodology. *Radiol Clin North Am.* 2001;39:997–1006.
21. Ziessman HA. Nuclear medicine hepatobiliary imaging. *Clin Gastroenterol Hepatol.* 2010;8:111–116.
22. Ziessman HA, Tulchinsky M, Lavely WC, et al. Sincalide-stimulated cholescintigraphy: a multicenter investigation to determine optimal infusion methodology and gallbladder ejection fraction normal values. *J Nucl Med.* 2010;51:277–281.
23. Liu N, Li M, Li X, et al. PET-based biodistribution and radiation dosimetry of epidermal growth factor receptor-selective tracer ^{11}C-PD153035 in humans. *J Nucl Med.* 2009;50:303–308.
24. Su H, Seimbille Y, Ferl GZ, et al. Evaluation of [^{18}F]gefitinib as a molecular imaging probe for the assessment of the epidermal growth factor receptor status in malignant tumors. *Eur J Nucl Med Mol Imaging.* 2008;35:1089–1099.
25. Riviere JEPM. Anesthetics and analgesics. In: *Veterinary Pharmacology and Therapeutics.* 9th ed. Hoboken, NJ: Wiley-Blackwell; 2009:247–248.
26. Moore AH, Cherry SR, Pollack DB, Hovda DA, Phelps ME. Application of positron emission tomography to determine cerebral glucose utilization in conscious infant monkeys. *J Neurosci Methods.* 1999;88:123–133.
27. Alkire MT, Haier RJ, Shah NK, Anderson CT. Positron emission tomography study of regional cerebral metabolism in humans during isoflurane anesthesia. *Anesthesiology.* 1997;86:549–557.